Calibrating Friction Coefficients in Discrete Element Method Simulations with Shear-Cell Experiments

Powder Technology 372 (2020) 290–304

Contents lists available at ScienceDirect

Powder Technology

journal homepage: www.elsevier.com/locate/powtec

Calibrating friction coefficients in discrete element method simulations with shear-cell experiments

Andrew Angus [a], Lyes Ait Ali Yahia [a], Riccardo Maione [a], Marv Khala [b], Colin Hare [b], Ali Ozel [a,*], Raffaella Ocone [a]

[a] School of Engineering and Physical Sciences, Heriot-Watt University, Edinburgh EH14 4AS, UK
[b] Department of Chemical and Process Engineering, University of Surrey, Guildford GU2 7XHK, UK

ARTICLE INFO

Article history:
Received 3 March 2020
Received in revised form 6 May 2020
Accepted 24 May 2020
Available online 11 June 2020

Keywords:
DEM
Torsional shear cell
Rolling friction
Sliding friction

ABSTRACT

Discrete Element Method (DEM) simulations coupled with shear cell experimental results have been used to investigate the flow behaviour of a dry particle assembly of glass beads in the quasi-static regime. Experimental studies have been undertaken using an FT4 powder shear cell apparatus, in parallel with extensive DEM simulations of both homogeneous simple shear and the FT4 shear cell itself. The findings show that it is not possible to accurately predict the bulk friction coefficient with homogeneous simple shear simulations unless both rolling and sliding friction are considered. There are, however, multiple pairs of sliding and rolling friction coefficients which can reproduce the experimental bulk friction coefficient. Sliding test experiments were conducted to yield the coefficient of sliding friction, and hence minimise the set of potentially correct pairs. Simulations of the full FT4 shear cell with two different calibration pairs, along with a pair without rolling friction, were then undertaken to understand the effect of their selection on realistic wall-bounded shearing conditions. Discrepancies were mainly found in the obtained radial contact number and velocity profiles, with increasing friction coefficients - particularly sliding friction - found to inhibit packing and particle velocity in the shear deformation zone. Comparison between homogeneous simple shear and shear cell simulation results showed a significant effect of the wall on the obtained force network, with almost a complete absence of the weakest structures which were seen supporting the strong structures in the simple shear scenario.

1. Introduction

Assemblies of granular particles such as sand or metal powders are ubiquitous in both nature and a wide range of engineering processes. The particles which make up these assemblies exhibit a broad range of intricate interactive behaviours that dictate the bulk behaviour of the granular media. These behaviours are dependent not only on the material, but also on the size and shape of the particles, and the presence of moisture. There is therefore a need for better understanding of complex particle-particle interactions at the particle-scale which will allow for accurate prediction of bulk behaviour. For granular materials there are two well-established regimes, inertial and quasi-static [5,44]. In the inertial regime, particle-particle collisions are instantaneous and binary, with flow analogous to a molecular gas [11,21]. Conversely, in the quasi-static regime - the focus of this study - flow is dense, and macroscopic deformation of granular material is slower compared with re-arrangement of particles at the microscopic scale. Movement of the particles in this regime is mainly driven by formation, rotation, and breakage of force chains. The flow behaviour of granular materials in the quasi-static regime has been extensively studied through experimental and computational means. Earlier experimental studies are focused on bulk behaviour (e.g. Schwedes [47]; Leturia et al. [38]), primarily using a shear cell with fixed lid and a base rotating around the vertical axis. Bridgwater et al. [9] showed that the velocity profile across the height of a narrow, densely packed powder bed (<20 particle diameters) is approximately linear, with slight deviation at the boundaries of the shear band and the neighbouring regions of unsheared powder above and below the band. Hsiau and Jang [27] employed particle tracking in a shear cell operating at higher strain rate and found a high shear region near the stationary cell wall, accompanied by a neighbouring low shear region near the moving wall which exhibited greater and more uniform velocity. Using the same cell arrangement, Hsiau and Yang [29] showed the velocity fluctuations in the direction of the flow to be much greater than in the transverse (vertical) direction, with an increase in solid fraction resulting in an increase in velocity fluctuation and a decrease in diffusion coefficients, whilst Hsiau et al. [28] showed that a reduction in friction coefficient results in an increase in shear rates and fluctuation velocities. More recent studies have used X-ray micro-tomography [4,7,8] and magnetic resonance imaging (MRI) [10,48] to provide experimental data at the particle-scale.

* Corresponding author.
E-mail address: a.ozel@hw.ac.uk (A. Ozel).

https://doi.org/10.1016/j.powtec.2020.05.079

Nomenclature

[L,01] C Number of contacts per particle
[L,02] $<C>$ Time-averaged local contact number
[L,03] C_{tot} Total number of contacts
[L,04] C_μ Damping coefficient for the EPSD model
[L,05] C_μ^{crit} Rolling critical viscous damping coefficient
[L,06] c Cohesion coefficient
[L,07] d_p Particle diameter
[L,08] F_c Contact force
[L,09] $<F_c>$ Mean contact force
[L,10] $F_{c,\,n}$ Normal component of contact force
[L,11] F_z^b Force exerted on the base of the shear cell, z component, simulations
[L,12] $F_{z,\,exp}^b$ Force exerted on the base of the shear cell, z component, experiments
[L,13] H_γ Height of the shear deformation zone
[L,14] I Inertial number
[L,15] I_i Moment of inertia related to particle i
[L,16] I_r Equivalent moment of inertia for two particles in contact
[L,17] K Proportional controller constant for the compression phase
[L,18] k_μ^{EPSD} Spring constant for the EPSD model
[L,19] k_μ^{EPSD2} Spring constant for the EPSD2 model
[L,20] k_n Normal spring constant
[L,21] k_tTangential spring constant
[L,22] M_r Rolling friction torque
[L,23] M_μ^d Rolling friction torque related to the dashpot in the EPSD model
[L,24] M_μ^s Rolling friction torque related to the spring in the EPSD model
[L,25] m_p Mass of a particle
[L,26]
[L,27] P Pressure
[L,28] $P(\psi)$ PDF of the branch unit vector angles
[L,29] $P(F_c)$ PDF of the contact force modulus
[L,30] $P_{objective}$ Objective Pressure
[L,31] R Radius of the shear cell
[L,32] R_c Shear head radius
[L,33] R_e Cylindrical vessel radius
[L,34] R_i Radius of the no-shearing zone in the shear cell
[L,35] R_r Ratio between k_μ^{EPSD} and k_μ^{EPSD2}
[L,36] r^* Equivalent radius
[L,37] T_z^t Torque exerted on the shear head, simulations
[L,38] $T_{z,\,exp}^t$ Torque exerted on the shear head, experiments
[L,39] $t_{compression}$ Duration of the compression phase during a HSS simulation
[L,40] t_{shear} Duration of the shearing phase during a HSS simulation
[L,41] $<U_s>$ Time averaged local solid velocity
[L,42] w_i^I Weight factor for the averaging procedure
[L,43] z Axial co-ordinate
[L,44] $\bar{z}$ Direction of the axial axes
[L,45] z_* Dimensionless axial co-ordinate
[G,01]
[G,02] $\dot{\gamma}$ Shear rate
[G,03] Δ Radial gap between the shear head and the cylindrical vessel
[G,04] Φ Solid volume fraction
[G,05] ε_{pp} Particle-particle restitution coefficient
[G,06] η_r Damping parameter for the EPSD model
[G,07] θ Azimuthal co-ordinate in cylindrical frame of reference
[G,08] $\tilde{\theta}$ Direction of the azimuthal axes in the cylindrical frame of reference
[G,09] θ_μ Relative rolling angle between two particles in contact
[G,10] $\dot{\theta}_\mu$ Relative rolling velocity between two particles in contact
[G,11] μ Particle-particle friction
[G,12] $<\mu^*>$ Time-averaged local coefficient of internal friction
[G,13] μ^* Internal friction coefficient
[G,14] μ_{exp}^* Internal friction coefficient observed experimentally
[G,15] μ_r Rolling friction
[G,16] μ^w Wall friction
[G,17] ν Poisson's ratio
[G,18] ρRadial co-ordinate in cylindrical frame of reference
[G,19] $\tilde{\rho}$ Direction of the radial axes in the cylindrical frame of reference
[G,20] ρ^* Dimensionless radial co-ordinate
[G,21] ρ_p Particle density
[G,22] σ_{ij} ij component of the stress tensor, HSS simulations
[G,23] σ^{zz} Normal stress, shear cell, simulations
[G,24] $\sigma^{zz,\,*}$ Dimensionless axial stress
[G,25] σ_{exp}^{zz} Normal stress, shear cell, experimental
[G,26] $\sigma\bar{z}_{exp,\,pre-shear}^{zz}$ Normal stress during pre-shear, shear cell, experimental
[G,27] $\sigma_{exp,\,shear}^{zz}$ Normal stress during shear, shear cell, experimental
[G,28] τ_{12} Major shear stress for HSS simulations
[G,29] $\tau^{\rho\theta}$ Shear stress on plane perpendicular to ρ, directed towards θ, simulations
[G,30] $\tau_{exp}^{\rho\theta}$ Shear stress on plane perpendicular to ρ, directed towards θ, experimental
[G,31] $\tau^{z\theta}$ Shear stress on plane perpendicular to z, directed towards θ, simulations
[G,32] $<\Phi_J>$ A macroscopic averaged property belonging to the mesh element J
[G,33] ϕ_i A macroscopic discrete property belonging to particle i
[G,34] ψ_n Direction of the branch vector
[G,35] Ω Shear head rotation velocity, simulations
[G,36] Ω_0 Shear head rotation velocity, test, simulations
[G,37] Ω_{exp} Shear head rotation velocity, experimental
[G,38] $\vec{\omega}_\mu$ Relative rotational velocity.

In terms of mathematical modelling, the Discrete Element Method (DEM) with a soft-sphere collision model [16] has been commonly used to investigate interaction between individual particles and predict bulk behaviour of granular materials in the quasi-static regime. For the soft-sphere collision model, particle-particle and particle-wall contact and damping forces are computed by either a linear (Hookean) or non-linear (Hertzian) spring-dashpot model, while sliding and rolling frictions are modelled with an additional torque and tangential force to resist rolling and sliding motions. In these models, particle-particle and particle-wall restitution coefficients, as well as sliding and rolling friction coefficients, need to be defined based on prior knowledge. Such knowledge has been historically difficult to determine experimentally. Restitution coefficients are commonly obtained via drop tests [14], while sliding inclined plane [18,36] and rolling resistance apparatus [25,26] have been used to provide limited insight into sliding and rolling friction respectively. Both these techniques are limited as they require a surface to be made of the particle material with identical roughness and composition to be sufficiently representative of particle-particle

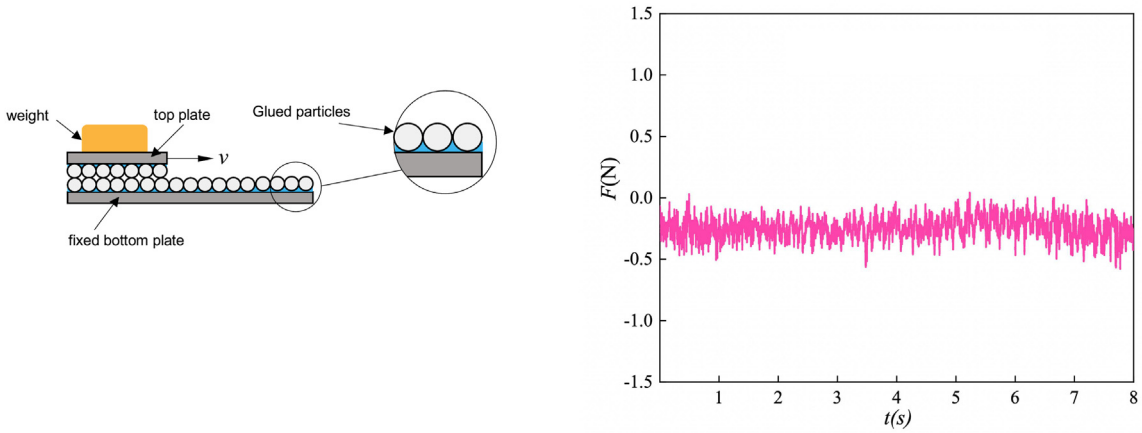

Fig. 1. (a) Schematic diagram of the sliding friction apparatus. (b) Time evolution of the sliding force F with a sliding speed equal to 5 mm/s and a weight W equal to 1.1 N.

interaction. A further technique which has been used is pile formation [24,54], with the angle of repose heavily dependent on rolling friction. Another technique which makes use of the angle of repose has been developed which analyses granular material in a continuously rotating drum [32]. Additionally, it is possible to study individual particles in contact at the molecular level using atomic force spectroscopy [39,52]. This technique, although accurate, is often prohibitively expensive. It is also limited to a maximum scanning area of 20 × 150 × 150μm, with multiple probes in parallel required if particle contact area exceeds this, raising both cost and complexity.

In this study, shear cell experiment results for internal friction of glass beads have been combined and compared with DEM simulations to measure bulk behaviour and determine possible rolling and sliding friction coefficient values. Measurement of the bulk friction coefficient in this way is well-established and highly accurate. Simultaneous calibration of both sliding and rolling friction is complex but it has been shown that, for spherical particles, DEM simulations accounting for only sliding friction are unable to predict the experimental bulk friction coefficient [34,42,50]. Coetzee and Els [15] conducted a similar calibration procedure to that of this work but accounted for only sliding friction, which was sufficient as non-spherical particles were used. Grima and Wypych [24] carried out the DEM calibration procedure using pile formation apparatus, and theorised that in the quasi-static regime the shape of non-spherical particles is sufficient to inhibit rolling without an additional resistant force being added to the model. For spherical particles, where the rolling friction is required, the calibration procedure can yield theoretically infinite possible correct combinations of sliding and rolling friction coefficients, and selection of the correct pair is the focus of discussion in this work. To reduce the number of potential pairs, a further sliding test experimental investigation was conducted to determine the sliding friction coefficient. In addition, the effect of selecting different potential calibration pairs on the results of simulating a realistic application has also been investigated.

The shear cell experiment subjects the granular material to a given applied normal pressure, and the stress needed to generate shear is evaluated. The shear cell apparatus of an automated powder rheometer is used in order to generate experimental shear test data (normal stress vs. shear stress and bulk internal friction coefficient). In addition, two types of DEM simulation have been performed: one with periodic domain Lees-Edwards (LE) boundary conditions, for the purpose of calibration; and one simulating the same shear cell geometry as the experimental apparatus. The shear cell simulations, while computationally expensive, allow a more detailed analysis on the effect of inter-particle friction coefficients on phenomena within a shear cell.

Table 1
Sliding test results.

Weight W[N]	Force F[N]	Sliding friction coefficient μ_{exp}
1.1	0.25 ± 0.079	0.23 ± 0.071
3.06	0.63 ± 0.19	0.21 ± 0.063

2. Experimental setup

2.1. Sliding test

The particles considered in this study are dry spherical glass beads with a diameter, d_p, of 500 μm. To determine the sliding friction coefficient, a mechanical sliding test was conducted using monolayers of these particles, which were glued onto a fixed bottom rectangular plate with dimensions of 40 mm by 150 mm and a top plate with dimensions of 40 mm by 40 mm. The glass particles were placed to form a tightly packed single layer that spans over plates. The two layers of particles were then brought into contact by applying a weight on the top plate as shown in Fig. 1a.

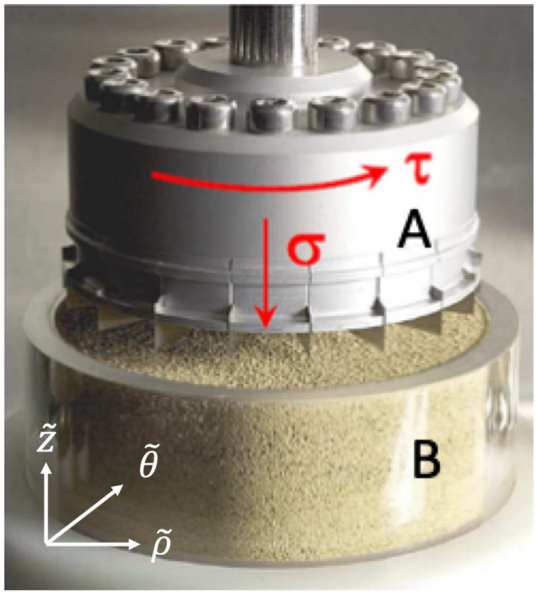

Fig. 2. FT4 shear cell: A - Shear head; B - Cylindrical cup. The direction of shear and normal stress are shown by τ and σ respectively.

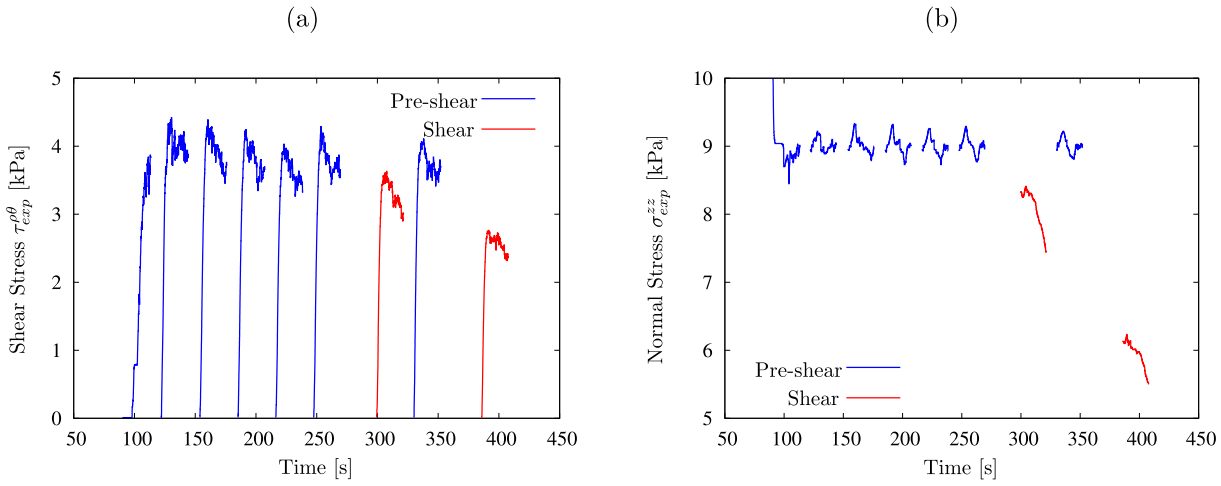

Fig. 3. Experimental procedure of FT4 shear cell, evolution of: (a) shear stress $\tau^{\rho\theta}_{exp}$ during pre-shearing and shearing phases. Normal stress σ^{zz}_{exp} and shear stress $\tau^{\rho\theta}_{exp}$ are evaluated by Eqs. (1) and (2), respectively; (b) normal stress σ^{zz}_{exp}.

A linear displacement-controlled drive moves the top plate in the horizontal direction and shears it against the bottom fixed plate at a controlled sliding speed. A 10 N load cell with a force resolution of 0.001 N is attached between the linear drive and the top plate to measure the force resulting from the sliding. The coefficient of sliding friction can then be evaluated as the ratio of sliding force F to the weight W.

Experiments were performed using two weights (1.1 and 3.06 N) and the sliding speed was fixed at 5 mm/s. Fig. 1-b shows the time evolution of the measured force F under a weight of 1.1 N. The presented results were averaged over 9 different measurements. The figure shows a steady evolution of the force in time with slight oscillations attributed to the small size of the particles. The forces were then averaged over time to compute the sliding friction coefficients μ_{exp}. The time-averaged force, weight and the corresponding sliding friction coefficients are given in Table 1.

2.2. FT4 rheometer shear cell

The flow behaviour of the glass bead assembly was evaluated using the shear cell test of the automated FT4 powder rheometer [20] (developed by Freeman Technology Ltd. Tewkesbury, Gloucestershire, UK). An image of the shear cell apparatus is presented in Fig. 2.

The shear head is a stainless steel cylinder (see Fig. 2, element A) with a radius, R_c, of 24 mm and equipped with 18 blades. These blades ensure that shearing occurs only between particles, without the influence of any wall effect related to shear-head–particle friction. The blades extend from the outer edge of the shear head to a point just outside the centre, leaving a central zone of radius, R_i= 3 mm in which particles do not shear. The cylindrical cup which holds the powder bed has an internal radius, R_e, of 25 mm. This system is capable of building the entire yield locus diagram of the analysed powder sample, and makes it possible to obtain several important properties such as the bulk friction coefficient μ^{*}_{exp}.

Angular velocity of the shear head is set to $\Omega_{exp} = 0.05$RPM and the experimental procedure begins with a pre-shear process. During the first pre-shear, the bladed shear head moves downward in order to apply a vertical consolidation stress (normal stress σ^{zz}_{exp}) on the powder bed (Fig. 2, element B). Once the desired normal stress is reached, the shear head starts to rotate and the resulting torque, M_z, $^{t}_{exp}$, is measured. The shear stress, $\tau^{\rho\theta}_{exp}$, and the consolidation stress are evaluated from the torque and the normal force applied by the shear head $F^{b}_{z,\,exp}$ respectively using the following relations:

$$\tau^{\rho\theta}_{exp} = \frac{3}{2}\left(\frac{M^{t}_{z,\,exp}}{\pi R_c^3}\right) \tag{1}$$

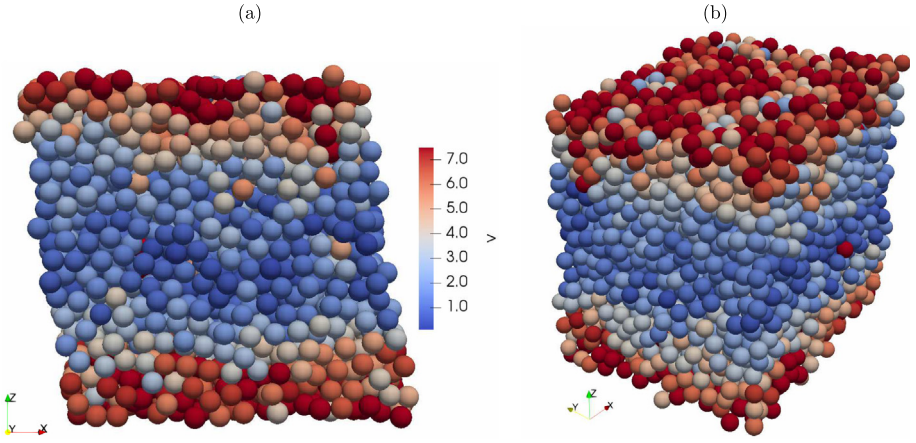

Fig. 4. Flow configuration of homogeneous simple shear: (a) - 2D rendering of a simulation showing normalised instantaneous particle velocity $v = \frac{|u_p|}{\dot{\gamma} d_p}$, where shearing takes place on the xz-plane; (b) - 3D rendering with dimensions [x y z] of $15 \times 15 \times 15$ d_p.

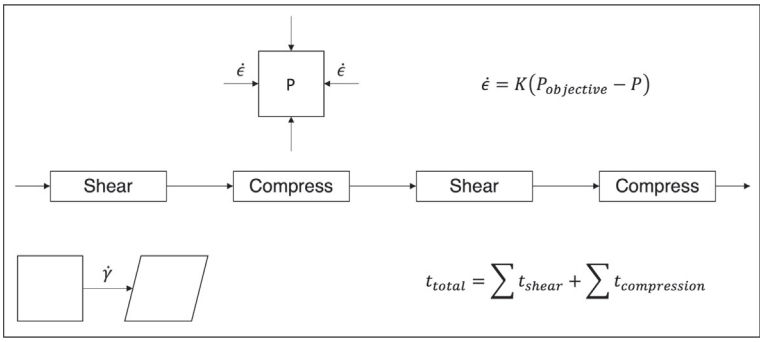

Fig. 5. Compression-shearing scheme for the homogeneous simple shear simulations to maintain the ratio of the desired pressure $P_{objective}$ and the evaluated applied pressure P at a value of one. The strain rate $\dot{\varepsilon}$ is dependent on the controller gain K, which defines the compression time $t_{compression}$.

$$\sigma^{zz}_{exp} = \left(\frac{F^{b}_{z,exp}}{\pi R_c^2}\right) \tag{2}$$

During the first pre-shear, the shear strength results and the shape of the curve (Fig. 3-a) are highly affected by the initial condition of the powder bed. This pre-shearing procedure is repeated until the maximum shear stress of two consecutive pre-shear steps show a difference of less than 1%. During every pre-shear, the normal pressure $\sigma^{zz}_{exp,\ pre-shear}$ is maintained constant (see Fig. 3-b) through a controller acting on the head of the shear cell. Once the powder reaches its critical state, the first shearing test is performed, normal pressure is set to the desired value and the shear strength of the material is evaluated using eq. (1). During a shearing test, the axial position of the shearing head is kept constant and the shear strength is considered as the peak of the shear stress curve. After every shear, another pre-shear step is executed to re-establish critical conditions. Shearing can then be repeated for several normal pressures to build the complete yield locus diagram.

For a conventional powder in the quasi-static regime, it is possible to represent the powder through the Mohr-Coulomb failure criterion. The shear stress $\tau^{\rho\theta}_{exp}$ is given by:

$$\tau^{\rho\theta}_{exp} = \mu^{*}_{exp}\sigma^{zz}_{exp} + c, \tag{3}$$

where c is the coefficient of cohesion. In this study, since particle size is sufficiently large, cohesive forces such as van der Waals are not significant and only the bulk friction coefficient μ^{*}_{exp} will be used for comparison with simulations.

3. Mathematical modelling

3.1. Contact model

For the simulations conducted in this study, the discrete element method (DEM) has been used. In the DEM approach [16], particles are tracked by solving Newton's equations of motion:

$$m_i\frac{d\boldsymbol{v}_i}{dt} = \sum_j\left(\boldsymbol{f}^{n}_{c,ij} + \boldsymbol{f}^{t}_{c,ij}\right) \tag{4}$$

$$I_i\frac{d\boldsymbol{\omega}_i}{dt} = \sum_j \boldsymbol{M}_{ij} + \boldsymbol{M}_r \tag{5}$$

In the equations, particle i is spherical and has mass m_i, moment of inertia I_i, translational and angular velocities $\boldsymbol{v}_i$ and $\boldsymbol{\omega}_i$. The normal and tangential contact forces between two particles i and j or particle i and wall j are represented by $\boldsymbol{f}^{n}_{c,\ ij}$ and $\boldsymbol{f}^{t}_{c,\ ij}$ respectively. The torque acting on particle i due to particle j is $\boldsymbol{M}_{ij}$ and $\boldsymbol{M}_r$ is the clipped torque due to rolling friction. $\boldsymbol{M}_{ij}$ is calculated as:

$$\boldsymbol{M}_{ij} = \boldsymbol{R}_{ij} \times \boldsymbol{f}^{t}_{c,ij}, \tag{6}$$

where $\boldsymbol{R}_{ij}$ is the vector from the centre of particle i to the contact point.

The particle contact forces $\boldsymbol{f}^{n}_{c,\ ij}$ and $\boldsymbol{f}^{t}_{c,\ ij}$ are calculated by following Johnson and Johnson [31] and Di Renzo and Di Maio [17] as:

$$\boldsymbol{f}^{n}_{c,ij} = k_n\delta_n^{3/2}\boldsymbol{n}_{ij} + 2\sqrt{\frac{5}{6}}\beta\sqrt{S_n m^*}\boldsymbol{v}^{n}_{ij} \tag{7}$$

$$\boldsymbol{f}^{t}_{c,ij} = \begin{cases} -8G^*\sqrt{r^*\delta_n}\boldsymbol{t}_{ij} + 2\sqrt{\frac{5}{6}}\beta\sqrt{S_t m^*}\boldsymbol{v}^{t}_{ij} & for \quad \left|\boldsymbol{f}^{t}_{c,ij}\right| < \mu\left|\boldsymbol{f}^{n}_{c,ij}\right| \\ -\mu\left|\boldsymbol{f}^{n}_{c,ij}\right|\dfrac{\boldsymbol{t}_{ij}}{\left|\boldsymbol{t}_{ij}\right|} & for \quad \left|\boldsymbol{f}^{t}_{c,ij}\right| \geq \mu\left|\boldsymbol{f}^{n}_{c,ij}\right|, \end{cases} \tag{8}$$

where;

$$\frac{1}{E^*} = \frac{1-\nu_i^2}{E_i} + \frac{1-\nu_j^2}{E_j} \tag{9}$$

$$\frac{1}{r^*} = \frac{1}{r_i} + \frac{1}{r_j}, \tag{10}$$

$$\beta = \frac{ln\,(e)}{\sqrt{ln^{\,2}(e) + \pi^2}} \tag{11}$$

$$S_n = 2E^*\sqrt{r^*\delta_n} \tag{12}$$

$$\frac{1}{G^*} = \frac{2(2+\nu_i)(1-\nu_i)}{E_i} + \frac{2(2+\nu_j)(1-\nu_j)}{E_j} \tag{13}$$

$$S_t = 8G^*\sqrt{r^*\delta_n} \tag{14}$$

$$m^* = \frac{m_i m_j}{m_i + m_j} \tag{15}$$

$$k_n = \frac{4}{3}E^*\sqrt{r^*} \tag{16}$$

The subscripts i and j denote spherical particle i and j respectively, and the superscript $*$ denotes the effective particle property of those two particles. Particle mass is denoted by m; E is Youngs modulus; G is the shear modulus; ν is Poissons ratio; r is particle radius; δ_n is normal overlap distance; $\boldsymbol{n}_{ij}$ represents the unit normal vector pointing from particle j to particle i; k_n is the normal spring constant; $\mathbf{v}^{n}_{ij}$ represents the normal velocity of particle j relative to particle i; $\boldsymbol{t}_{ij}$ represents the tangential displacement obtained from the integration of the relative tangential velocity during the contact, $\boldsymbol{v}^{t}_{ij}$; and μ is the particle sliding

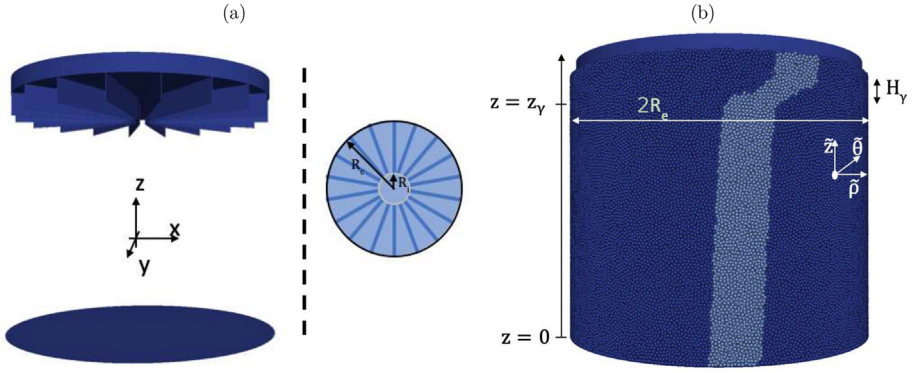

Fig. 6. Shear Cell flow configuration: (a) - Wall mesh showing key radii of the shear head as well as axis labels [*xyz*] for ready comparison with Lees Edwards simulations; (b) - Rendering of a shear cell simulation with particles coloured white to highlight the shear deformation zone. The vectors $(\tilde{\rho},\tilde{\theta},\tilde{z})$ represent the directions of the cylindrical frame of reference.

friction coefficient. The model developed by Ai et al. [3] is used to account for rolling friction (often called the Elasto-Plastic Spring Dashpot (EPSD) model):

$$\boldsymbol{M}_r = \boldsymbol{M}_r^k + \boldsymbol{M}_r^d \tag{17}$$

This model consists of spring torque, $\boldsymbol{M}_r^k$, and viscous damping torque, $\boldsymbol{M}_r^d$, components, analogous with the contact force model. The spring torque is evaluated with an incremental approach:

$$\Delta\boldsymbol{M}_r^k = -k_r^{EPSD}\Delta\boldsymbol{\theta}_r \tag{18}$$

$$k_\mu^{EPSD} = 2.25k_n\mu_r^2 r^{*2} \tag{19}$$

$$\boldsymbol{M}_{r,t+\Delta t}^k = \begin{cases} \boldsymbol{M}_{r,t+\Delta t}^k = \boldsymbol{M}_{r,t}^k + \Delta\boldsymbol{M}_r^k \\ |\boldsymbol{M}_{r,t+\Delta t}^k| \le \mu_r r^* \boldsymbol{f}_{c,ij}^n, \end{cases} \tag{20}$$

where θ_r and k_r^{EPSD} are the relative rotation and the rolling stiffness respectively. With regards to the dashpot component:

$$\boldsymbol{M}_{r,t+\Delta t}^d = \begin{cases} -C_r\dot{\boldsymbol{\theta}}_r & \text{if} \quad |\boldsymbol{M}_{r,t+\Delta t}^k| < \mu_r r^* \boldsymbol{f}_{c,ij}^n \\ -fC_r\dot{\boldsymbol{\theta}}_r & \text{if} \quad |\boldsymbol{M}_{r,t+\Delta t}^k| = \mu_r r^* \boldsymbol{f}_{c,ij}^n, \end{cases} \tag{21}$$

where f is a tuneable parameter between 0 and 1 which defines the fraction of energy dissipation due to viscous damping (in this case set to 1). $\dot{\boldsymbol{\theta}}$ is the relative rolling velocity and the rolling viscous damping constant, C_r, is evaluated through the set of equations:

$$C_r = -\eta_r C_\mu^{crit} \tag{22}$$

$$C_r^{crit} = 2\sqrt{I_r k_r^{EPSD}} \tag{23}$$

$$I_r = \left[\frac{1}{I_i + m_i r_i^2} + \frac{1}{I_j + m_j r_j^2}\right]^{-1}, \tag{24}$$

where η_r, C_μ^{crit} and I_r are the rolling viscous damping ratio, critical damping constant, and the equivalent moment of inertia for two particles in contact, respectively. I, m and r, with both subscript i and j, are the moment of inertia, the mass, and the radius of particle i and j, respectively. In this study, the value of η_r is considered to be 0.3 as given by Ai et al. [3], unless otherwise stated. The given equations are numerically solved with an open source software, LIGGGHTS (LAMMPS for Improved General Granular and Granular Heat Transfer Simulations) [23,35].

Table 2
Particle properties and DEM model parameters for homogeneous simple shear reference case.

Parameter	Value
Restitution coefficient ε_{pp}	0.9
Radius r_p	250 μm
Density ρ_p	2500 kg/m^3
Poisson's ratio ν	0.3
Sliding friction coefficient μ	0.25
Rolling friction coefficient μ_r	0.0

4. Flow configurations

4.1. Homogeneous simple shear simulations

Homogeneous simple shearing (HSS) of granular material in a periodic cuboid box with Lees-Edwards (LE) boundary conditions [37] was the first flow configuration studied in this work. The shearing plane (*xz*) is shown in Fig. 4-a, while 4-b illustrates the cubic domain of dimensions $15 \times 15 \times 15\ d_p$. Both figures show normalised particle velocity and it can clearly be seen that shearing is imposed on the top and bottom of the domain, uniformly across the *xy*-plane.

For these simulations, the pressure P is maintained constant by adjusting the simulation box dimensions while shearing. The particle stress tensor, $\boldsymbol{\sigma}$, in the domain is computed as:

$$\boldsymbol{\sigma} = \frac{1}{V}\sum_i \sum_{j\neq i} \frac{1}{2}\boldsymbol{r}_{ij} \otimes \boldsymbol{f}_{c,ij}, \tag{25}$$

where $\boldsymbol{r}_{ij}$ is the centre-to-centre contact vector from particle j to particle i, $\boldsymbol{f}_{c,ij}$ is the total contact force between the two particles and V is the domain volume. Since the kinetic part of the stress tensor is very small compared with the collisional part in this study, it is neglected in eq. (25). The pressure is then evaluated by:

$$P = \frac{1}{3}\mathrm{Tr}\boldsymbol{\sigma}. \tag{26}$$

To maintain constant pressure in the domain, a control loop is defined with successive shearing and compression phases as shown in Fig. 5. In the shearing phase, the granular material is sheared with a

Table 3
Bulk friction coefficient μ^* as a function of shear rate $\dot{\gamma}$ and inertial number I with simple shear simulations. Particle properties are given in Table 2. Number of particles is equal 6000 and Young's modulus is equal to 0.025 GPa.

$\dot{\gamma}$ [s^{-1}]	I	μ^*
0.00252	9.11×10^{-7}	0.335 ± 0.012
0.0126	4.56×10^{-6}	0.337 ± 0.011
0.0252	9.12×10^{-6}	0.336 ± 0.009

Table 4
Solid volume fraction ϕ, coefficient of internal friction μ^*, and contact number C, as a function of number of particles N with simple shear simulations. Young's modulus is equal to 0.025 GPa and shear rate is equal to 0.0252 s^{-1}.

N	μ^*	ϕ	C
2000	0.3369 ± 0.0147	0.6080 ± 0.0014	5.3791 ± 0.0311
4000	0.3361 ± 0.0115	0.6082 ± 0.0009	5.3719 ± 0.0247
6000	0.3363 ± 0.0092	0.6084 ± 0.0009	5.3780 ± 0.0196

constant shear rate $\dot{\gamma}$ for time t_{shear} while system pressure is monitored. Following this phase is the compression phase, where pressure is re-adjusted to the objective value $P_{objective}$ using a proportional controller, and the cycle is repeated. The compression time $t_{compression}$ is dependent on the strain rate, $\dot{\varepsilon}$, which is adjusted according to the controller gain, K. This procedure ensures that P is accurately maintained throughout the shearing process, with the dimensionless pressure $P/P_{objective}$ equal to 1 ± 0.002. There is the potential, however, that high shear rates could affect pressure stability and compression times. The duration of the simulation is set to $11/\dot{\gamma}$ which is sufficient to let the system attain steady state and to obtain statistically converged data.

Since it is desired to operate in the quasi-static regime, the shear rate needs to be chosen accordingly through the inertial number, I [33]:

$$I = \dot{\gamma}\sqrt{\frac{m_p}{d_p P}}, \tag{27}$$

where m_p represents the mass of a single particle. For $I < 1 \times 10^{-3}$, the granular system is in the so-called quasi-static regime [2,6,33,43], in which the bulk friction coefficient, μ^*, becomes independent of shear rate and is calculated as:

$$\mu^* = \frac{\tau^{zx}}{P}. \tag{28}$$

4.2. FT4 shear cell simulations

DEM simulations of the glass beads in the FT4 shear cell have also been performed at exact geometric scale as the experiment. Fig. 6-a shows the computational domain, with the DEM geometry for the experimental apparatus (shear cell walls are omitted for the sake of clarity). A difference of note between the experimental and simulated shear cells is in the application of normal and shear stress, with the base being used to apply normal stress and the shear head used to apply shear stress in the simulations.

In Fig. 6-b, a rendering of particles in a shear cell simulation is presented, showing the key dimensions and axis direction labels. To let the particle bed expand without building up pressure inside the shear cell, there is a small radial gap between the shear head and the cylindrical cup $\Delta R = R_e - R_c = 1$ mm. The shear deformation zone is limited to only a small band of height, H_γ (~$10d_p$), beneath the shear head blades, with the rest of the particle bed contributing little to the simulation environment.

Table 5
Solid volume fraction ϕ, coefficient of internal friction μ^*, contact number C, and binary collision time t_{bc} as a function of Young's modulus E for simple shear simulations. Number of particles equals 4000, and shear rate is equal to 0.0252 s^{-1}.

E [GPa]	ϕ	μ^*	C	t_{bc} [s]
2.5	0.599 ± 0.001	0.337 ± 0.015	4.611 ± 0.027	5.35×10^{-5}
0.25	0.600 ± 0.001	0.334 ± 0.012	4.872 ± 0.026	1.34×10^{-4}
0.025	0.608 ± 0.001	0.336 ± 0.012	5.372 ± 0.025	3.37×10^{-4}

The shear cell simulations are divided into an initial compression phase and a shearing phase. In the compression phase, particles are arbitrarily located in the shear cell and the base moves upward along the cylinder axis until the objective normal stress is attained. This is done while maintaining the wall friction coefficient between the particles and the cylindrical vessel, μ^w, equal to zero, ensuring particles in the shearing zone attain the desired pressure without any losses to the surrounding walls. During the shearing phase, wall friction is activated and the shear head rotates at a constant rate, Ω, while the pressure is maintained at $P_{objective}$ via compression applied by the base. The shear rate, $\dot{\gamma}$, is evaluated as:

$$\dot{\gamma} \approx \frac{\Omega R_c}{2H_\gamma}, \tag{29}$$

The normal stress, σ^{zz}, parallel to the cylinder axis, the shear stress, $\tau^{\rho\theta}$, and the bulk friction coefficient are evaluated with the following relationships:

$$\sigma^{zz} = \frac{F_z^b}{\pi R_c^2} \tag{30}$$

$$\tau^{\rho\theta} = \frac{3}{2}\frac{M_z^t}{\pi R_c^3} \tag{31}$$

$$\mu^* = \frac{\tau^{\rho\theta}}{\sigma^{zz}} \tag{32}$$

where F_z^b is the force in the z direction recorded at the bottom of the shear cell, and M_z^t is the torque applied by the shear head on the glass beads. F_z^b and M_z^t are evaluated by integrating the force applied on each mesh element of the wall. Due to the high computational expense of these simulations they were only run until statistically converged data was obtained, which equated to 7 s of real time, with the first 2 s neglected for analysis.

5. Results and discussion

In this section, we first report a parametric study of simple shear simulations. In these simulations, we varied DEM parameters, the applied pressures and shear rates and investigated if they had any significant effect on the flow field. Then, the chosen parameters were used to study the effect of inter-particle friction coefficient pairs on homogeneous simple shear and shear cell simulations.

5.1. DEM parameters of reference case

Before proceeding with the objectives of this work, a parametric study was conducted in which shear rate, number of particles N, and Young's modulus E were varied for LE simulations. This was done to see the effect on predictions of bulk friction coefficient, and in the case of number of particles and Young's modulus, also on contact number, C, and solid volume fraction, ϕ. The particle properties used for the parametric study are presented in Table 2, and the pressure, $P_{objective}$, was set to 5 kPa. This pressure was chosen following simulations using pressures of 5 and 8 kPa, where no difference was found in bulk friction coefficient results.

To make sure the numerical simulations belong to the quasi-static regime, three simulations with different shear rates were chosen: $\dot{\gamma} = 0.00252\ s^{-1}$, $\dot{\gamma} = 0.0126\ s^{-1}$, and $\dot{\gamma} = 0.0252\ s^{-1}$. These correspond to inertial numbers of 9.11×10^{-7}, 4.55×10^{-6}, and 9.11×10^{-6} respectively.

Table 3 reports the predicted μ^* for the three different shear rates. One can see that the bulk friction coefficients differ less than the statistical uncertainty, and the property is therefore independent of shear rate and inertial number, as is expected for the quasi-static regime. A

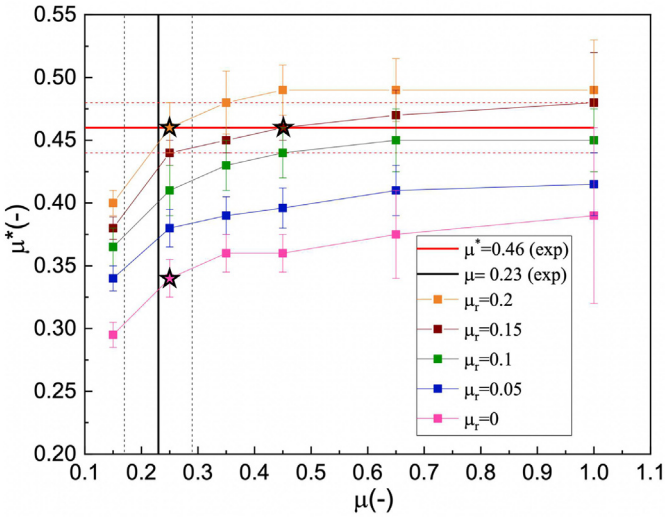

Fig. 7. Bulk friction coefficient μ^* as a function of the sliding friction μ and rolling friction μ_r, plotted against the experimentally obtained coefficient of internal friction μ^*_{exp}. The star symbols show the friction coefficient pairs (μ, μ_r = 0.25,0.2; 0.25,0; 0.45,0.15) that are used for the rest of the study.

value of $\dot{\gamma} = 0.0252\ s^{-1}$ was selected for all subsequent simulations in this work. This shear rate value could be further increased - reducing computational time - since the inertial number is low, however $\dot{\gamma}$ also has an important effect on the stability of the LE algorithm as described in Section 4.

As investigated by Peyneau and Roux [43], the number of particles can also have an effect on the simulation results. Too small a system could interfere with the applicability of periodic boundary conditions, and too large a system becomes computationally expensive. Hence, the behaviour of the system with three numbers of particles was investigated: $N = 2000$, $N = 4000$, and $N = 6000$. The results for the bulk friction coefficient as a function of number of particles in the system, along with the solid volume fraction and the contact number are presented in Table 4.

It was found that differences in obtained results for all the aforementioned variables varied much less than the experimental uncertainty for each number of particles used. No significant impact on mean result is therefore exhibited, however the standard deviations of obtained results decreased slightly with increasing particle number. To give good balance between statistical certainty and computational cost, a particle number of $N = 4000$ was therefore chosen for all subsequent simulations.

The Young's modulus, E, determines the particle overlapping distance and collision duration. Consequently, the force network, coordination number, and solid volume fraction can be altered. The results showing these effects are available in Table 5. Selection of a time-step for DEM simulations which allows correct integration of contact interactions is important, and good choice of this parameter can increase the efficiency of the simulation significantly. A time-step equal to 2% of the binary collision time, t_{bc}, is recommended [1], which is calculated for the Hertzian collision model as [51]:

$$t_{bc} = 2.943\left(\frac{5\sqrt{2}\pi\rho(1-\nu^2)}{4E}\right)^{2/5}\frac{r_p}{v_0^{1/5}}, \tag{33}$$

where v_0 is the characteristic velocity:

$$v_0 = \dot{\gamma}\, d_p \tag{34}$$

It can be seen that only contact number and collision time vary significantly with Young's modulus. These artificial effects are given by the high overlaps attained with a small Young's modulus. The real Young's modulus of glass is significantly higher than all values tested, but would be too computationally expensive to use. It should also be noted that a higher Young's modulus with a stiffer response slightly decreases the stability of the result for μ^*.

Inertial number is not the only variable which defines the boundary of the quasi-static regime. Critical solid volume fraction, ϕ_c, and critical contact number, C_c, are also given as boundary conditions [13,49]. The values for this case ($\mu = 0.25$) are $\phi_c \approx 0.598$ and $C_c \approx 4.69$. While all values of E satisfy the first condition, the high Young's modulus case fails to meet the contact number criterion. A value of E = 0.25 GPa was chosen to retain reasonable accuracy while reducing computational expense and erring on the side of caution with respect to critical contact number.

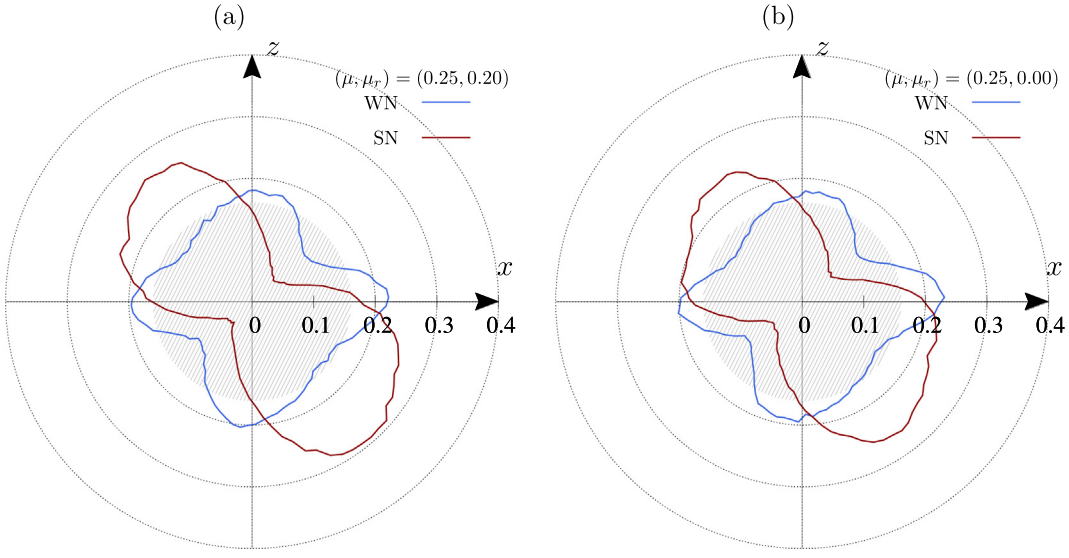

Fig. 8. Polar diagrams of the probability density function of the branch vector directions on the xz-plane, for the strong network (SN) and the weak network (WN) with homogeneous simple shear simulations for two friction coefficient pairs: (a) - $\mu = 0.25$ and $\mu_r = 0.20$; (b) - $\mu = 0.25$ and $\mu_r = 0.00$. The shaded area represents an isotropic distribution.

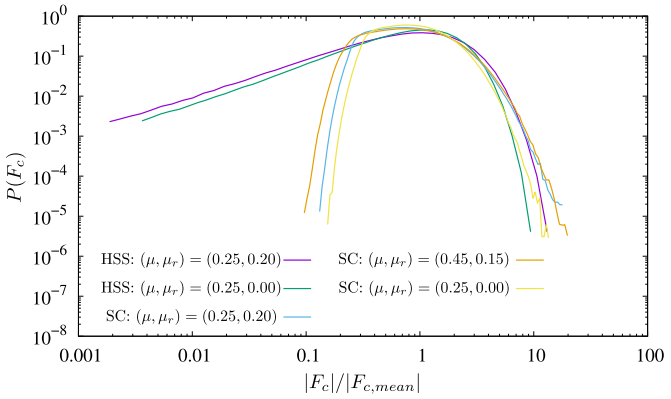

Fig. 9. Comparison between the contact force PDFs obtained with the HSS approach and the contact forces PDFs obtained with the shear cell approach in the shear deformation zone for relevant inter-particle friction coefficient pairs.

5.2. Rolling friction effect on homogeneous simple shear simulations

In order to improve the computational efficiency of DEM simulations, the interaction models are simplified. This is why DEM model parameters are often calibrated to match the response of an experimental system [12]. In this case the calibration will consist of tuning inter-particle friction coefficients (μ, μ_r) to reproduce the coefficient of internal friction μ^*_{exp} measured with the experimental apparatus illustrated in section 2. The particle properties and simulation parameters used remain the same as in the reference case, with only the coefficients of sliding friction and rolling friction varied.

A total of 30 simulations with the EPSD model have been run using different friction coefficients pairs. Other rolling friction models commonly used in DEM simulations have also been tested, with the results available in appendix 7.1. Fig. 7 shows the internal friction coefficient, μ^*, given by LE simulations as a function of the sliding friction, μ, and rolling friction, μ_r. The experimental coefficient of internal friction ($\mu^*_{exp} = 0.46 \pm 0.02$) obtained with the shear cell measurements is also shown in the graph, together with the experimental mean sliding friction coefficient ($\mu_{exp} = 0.23$).

For each value of μ_r, the coefficient of internal friction μ^* increases as a function of μ at an exponentially decreasing rate. It can also be seen that the stability of the internal friction result decreases with increasing μ. When the effects of rolling friction are neglected, μ^* approaches a plateau [6,19,40,53] at a value far from the one measured experimentally for the glass beads ($\mu^*_{exp} = 0.46 \pm 0.02$). Rolling, as can be seen in several other works [3,19,30,34], is important in increasing the shear strength of the granular material and its inclusion is necessary to reach μ^*_{exp}. Considering the sliding test results ($\mu_{exp} = 0.23$), the rolling friction coefficient must have a value of ~0.20 to accurately predict the coefficient of internal friction, assuming that sliding friction alone is responsible for the measured shear force in the sliding tests. Since the simulated particles are perfectly smooth then if this setup were to be simulated using the determined sliding friction coefficient based on these highly spherical particles, then the simulated sliding force is likely to be slightly less than that of the experiment. There will also be a slight discrepancy due to the very narrow size distribution of the real material, which is not simulated. Nevertheless, we consider these effects to be minor and so equate μ_{exp} to μ_s.

It is worth noting that there is a large set of rolling and sliding friction pairs capable of reproducing μ^*_{exp}. If one of these coefficients is unknown, the calibration procedure is not univocal anymore. To investigate how these coefficients alter flow dynamics in detail, another calibration pair (μ, μ_r) = (0.45, 0.15) which produces the same coefficient of internal friction was used, along with a pair excluding rolling friction (μ, μ_r) = (0.25, 0.00), for further analyses discussed below.

The inclusion of a rolling friction model does not only have an impact on results for bulk friction coefficient. In shearing granular media it is well known that is possible to distinguish between two types of force network [19,53,45]: a strong force network formed by particles experiencing forces above the average; and a weak force network, formed by particles experiencing forces below the average. These two networks are known to have very different roles in the particle system, with the strong network (SN) almost completely oriented in the major stress direction. The weak network (WN) is then almost isotropic and has the function of stabilising the strong network while mainly contributing to the mean pressure [46]. The rolling friction greatly affects these stress transmission patterns in granular media as observed by Estrada et al. [19] for the shearing of 2D disks.

It is possible to extrapolate the main direction of the contact vectors to discover the orientation of the principal networks. This has been done by evaluating the probability density function (PDF) $P(\psi n)$ of the branch unit vector angles $\psi_n \in [-\pi, \pi]$ on the xz-plane during the shearing phase at steady state. Branch vectors were categorised into WN and SN based on the normalised contact force $|F_c| / |F_{c,mean}|$, which if ≤1 signified a WN contact, and if >1 signified a SN contact. The PDF was constructed using 150 time-steps and >1 million contacts, with contact vectors larger than d_p ignored. Contact vectors larger than d_p are an artificial effect of using a reduced Young's modulus, with unrealistic weak contacts created by particle deformations.

The results are shown in Fig. 8-a and 8-b for (μ, μ_r) = (0.25, 0.00) and for (μ, μ_r) = (0.25, 0.20) respectively. It should also be noted that the pair (μ, μ_r) = (0.45, 0.15) showed identical branch vector distributions to (μ, μ_r) = (0.25, 0.20).

One can see that the SN tends to orient in the direction of the major stress, while the WN main directions are parallel to the main axes of compression. These results further demonstrate that the roles of the two networks are different. We also see, however, that for the pairing with a higher shear resistance (Fig. 8-a) the anisotropy of the strong network is higher than the other pairing (Fig. 8-b). By following the work of Estrada et al. [19], there should be a value of shear strength for which the WN starts to orient towards the shearing direction like the SN, but this was not seen with these HSS simulations.

While these results provide physical insight concerning the flow dynamics, they show no difference in potential inter-particle coefficient pairs. To highlight the impact of selection of pairs in a realistic application, simulations of the full FT4 shear cell were also conducted. The conditions of the LE simulations are different from the ones used in the FT4 shear cell experiments in a number of ways. These include linear homogeneous shearing, periodic boundary conditions (no wall effect), and reduced particle number. It was also hoped these additional simulations would shed valuable light on the particle-scale dynamics of a shear test.

5.3. Shear cell simulations - effect of the inter-particle friction coefficient pairs

In this section, the effects generated by inter-particle friction coefficient selection on the results of shear cell simulations will be investigated. Aspects investigated will include main internal structure of the FT4 shear cell, as well as results for bulk friction, local friction, particle velocity, and contact number. The parameters used for the simulations are mostly the same as for HSS simulations. Differences include particle number increasing to 800,000 and shear rate being set by shear head rotation speed, which will be discussed later. An additional parameter input required for the shear cell simulations was the wall friction coefficient, μ^w, between particles and the cylindrical vessel wall. The effect of the choice of wall friction was investigated and can be found in appendix 7.2, with the results showing that a minimum value of wall friction was necessary to stop singular block rotation of the particle bed. It was also found that too high a value produced sharp reductions in the dimensionless normal stresses in the shear zone approaching the wall.

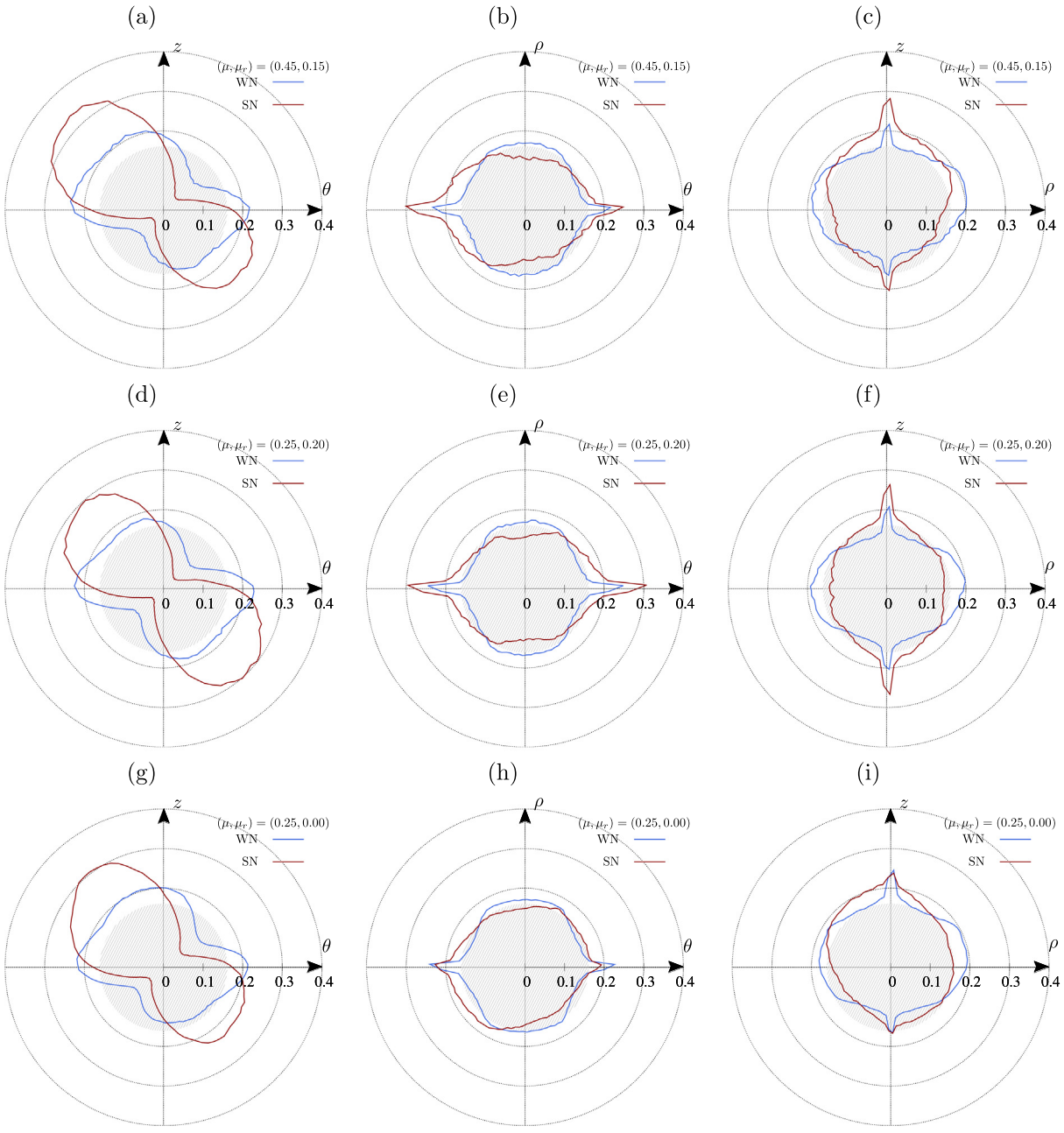

Fig. 10. Polar diagrams of the probability density function of the branch vector directions on the 3 planes for the strong network (SN) and the weak network (WN) for shear cell simulations. (a)–(c): $(\mu, \mu_r) = (0.45, 0.15)$. (d)–(f): $(\mu, \mu_r) = (0.25, 0.20)$. (g)–(i): $(\mu, \mu_r) = (0.25, 0.00)$. The shaded areas represents an isotropic distribution.

A value of $\mu^w = 0.1$ was then chosen for use in the simulations in this section to give good balance between these two constraints.

Three simulations were performed where the friction pairs were $(\mu, \mu_r) = (0.45, 0.15)$, $(\mu, \mu_r) = (0.25, 0.20)$ and $(\mu, \mu_r) = (0.25, 0.00)$. These represent the two calibration pairs yielded from section 5.2, as well as an incorrect pair which does not account for rolling friction. The rotation speed, Ω, used for these simulations was higher than the one used in experiments Ω_{exp}. This was done to increase the speed of the simulations, which would otherwise be prohibitively expensive. For $\Omega = 3$RPM, the inertial number I is equal to 3×10^{-4}, which should ensure that the system lies in the quasi-static regime. Nonetheless, to prove this hypothesis, another simulation was run with $\Omega_0 = 1$RPM. No change was observed in μ^* when changing the speed from Ω to Ω_0, further proving that the granular material for this speed is in the quasi-static regime. Considering $\Omega_{exp} = 0.05$RPM, and the increased speed simulations still took ~2 weeks on 28 CPUs to simulate 7 of real-time, it can be clearly seen why this step was taken.

The internal structures of the shear cell simulations for each pair were compared with each other, and also with those obtained with the HSS simulations. Fig. 9 shows the force network PDF $P(F_c)$ for each case, which gives the distribution of normalised contact forces in the shear deformation zone with artificial contacts (contact vector $> d_p$) ignored as in section 5.2. A logarithmic binning procedure was also employed to ensure the weakest forces were effectively captured.

In general, the WN represents most of the contacts in the force network while the SN represents only a small part for HSS simulations. Only one of the calibration pairs is given for these simulations as they had identical distributions. Rolling friction does not alter the general shape of the PDF, however the effect of rolling friction is clearly visible and gives a more isotropic distribution for both HSS and shear cell

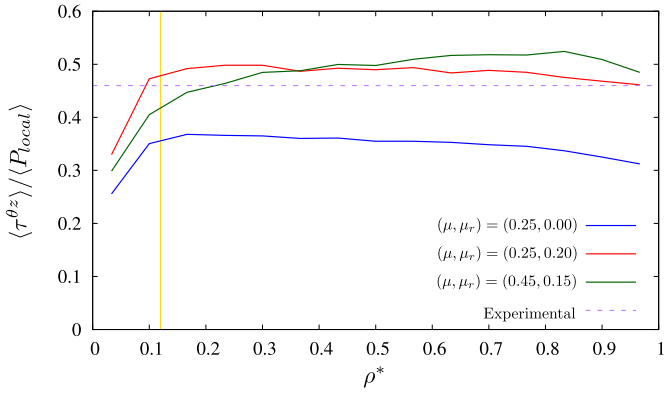

Fig. 11. Time-averaged local coefficient of internal friction $\frac{\langle \tau^{\theta z} \rangle}{\langle P_{local} \rangle}$ as a function of the dimensionless radial co-ordinate ρ^* for different inter-particle friction coefficient pairs, compared with the coefficient of internal friction obtained from experiments. The yellow line represents the boundary of the central "no-shearing" zone. (For interpretation of the references to colour in this figure legend, the reader is referred to the web version of this article.)

simulations. When increasing rolling friction there is a decrease in particles belonging to the "mean" network and an increase in particles belonging to the strong and weak contact networks. This is logical as increasing the shear strength of the system increases the likelihood of the system to form strong force chains that carry almost all the load applied to the granular assembly.

It can be seen that there is a clear difference in the WN values found with the shear cell simulations, when compared with the HSS simulations. In fact, in the shear cell simulation there is almost a complete absence of the weakest structures, while the strong network shows a similar distribution to HSS simulations. The absence of the weak network is probably due to the presence of the wall, which takes on the role of stabilising the strong force chains. Supporting this hypothesis, most of the weak network is concentrated in the central "no-shearing" zone, as well as a small part near the cylindrical cup.

Fig. 10 shows the branch vector distribution $P(\psi)$ on the three principal planes for each shear cell simulation pair. The co-ordinate system was converted from Cartesian to cylindrical to analyse the branch vector directions ψ_n. For comparison with $P(\psi)$ for HSS simulations in Fig. 8, the plane-xz is equivalent to plane-θz in these diagrams (Figs. 10-a,d,g). It can be seen that the shape of the strong network in this plane is very similar to what was obtained before, particularly for the pair $(\mu,\mu_r) = (0.25,0.20)$. It is orientated in the direction of the major stress and would seem to confirm the notion that the SN is more or less unchanged in the shear cell simulations, as was seen in Fig. 9. Also as before with the HSS simulations, the case without rolling friction has a notably less isotropic distribution for the strong network. A difference of note in this plane between the simulation methods, is that the weak network can also be seen to orient in the direction of the major stress, perhaps confirming its loss of the role of support network.

The branch vector distributions on two other planes were also investigated, plane-$\theta\rho$ (Figs. 10-b,e,h) and plane-ρz (Figs. 10-c,f,i). It can be seen that for the 'correct' $(\mu, \mu_r) = (0.25, 0.20)$ and the 'potential' $(\mu, \mu_r) = (0.45, 0.15)$ pairs, the strong networks are orientated in the angular and compression axes respectively, while the pair without rolling friction shows more of a radial orientation. This is possibly due to the fact without rolling friction the particles are prone to movement in directions other than that of the shear rotation. It can also be seen that for the friction coefficient pair $(\mu,\mu_r) = (0.45,0.15)$ the SN distributions are asymmetrical and favour more the direction of shear head rotation and upward on the z-axis towards the shear head itself. This is possibly due to the increased sliding friction of particles showing a greater tendency to be dragged along with the shear head and the particles driven between the blades causing shear.

The WN for all pairs on these planes show similar distributions, with those on the plane-$\theta\rho$ approaching isotropy and those on the plant-ρz orientating slightly along the radial axis counter to the orientation of the SN on the compression axis. A final observation is the 'correct' pair $(\mu,\mu_r) = (0.25,0.20)$ is the only pair to show symmetrical distributions with axial orientation on the two radial planes. This is an aspect which may warrant further investigation with other particle systems to possibly establish this as a numerical method to identify the 'correct' friction coefficient pair following HSS simulations.

An averaging utility that allows mapping particle properties onto a three-dimensional mesh was used to obtain locally-averaged results for contact number, stress, and velocity in the shear deformation zone. To perform a mesh convergence study, four mesh element sizes were studied: mesh 1:7 d_p cell size; mesh 2:5.1 d_p cell size; mesh 3:3.9 d_p cell size; mesh 4:3.2 d_p cell size. The mesh which was chosen as a result of the convergence study was that with cubic cells of length equal to 3.2 d_p. The averaging utility assigns each particle i to the mesh element J with a weighting function w_i^J. It is then possible to average a generic macroscopic discrete property Φ_i for every mesh element through the following equation:

$$<\Phi_J> = \frac{\sum_{i=1}^{N} w_i^J \Phi_i}{\sum_{i=1}^{N} w_i^J}, \tag{35}$$

where $<\Phi_J>$ is the local average value of the generic discrete property Φ in the mesh element J. These properties were calculated for every time-step and used to create time-averaged properties $\langle \Phi_J \rangle$ for each mesh element, and finally these properties were averaged over the θz-plane in the shear deformation zone to yield radial distributions of the properties of the form ' $\langle \Phi \rangle$ '. The radial evolution of the local friction coefficient $\langle \tau^{\theta z} \rangle$ / $\langle P_{local} \rangle$ in the shear deformation zone is shown in Fig. 11. It is given as a function of the dimensionless radial coordinate $\rho^* = \frac{\rho}{R_e}$. The time-averaged non-local normal pressure $\langle P_{local} \rangle$ is calculated as:

$$\langle P_{local} \rangle = \frac{1}{3} \mathrm{Tr} \ \langle \sigma \rangle \tag{36}$$

For low values of ρ_* (up to $\rho_* = 0.12$), the system is in the œnoshearing zone, where blades do not induce any shear on particles. In this part of the system, $\frac{\langle \tau^{\theta z} \rangle}{\langle P_{local} \rangle}$ is low, but it rapidly reaches a value of μ^* similar to that observed with HSS simulations. This is not surprising, since μ^* represents the failure criterion for glass beads in the quasi-static regime; hence, for $\rho^* < 0.12$ the granular material behaves like a rigid solid, while for $\rho^* > 0.12$ it behaves like a plastic. Averaging over the radial axis yields an estimate for bulk friction coefficient and the results obtained in this way are shown in Table 6, along with the values predicted by eq. (32) and HSS simulations. It can be seen that there is good agreement between the HSS simulations predictions and the predictions using the local friction method for shear cell simulations. This

Table 6
Comparison of bulk friction coefficient results using homogeneous simple shear (HSS) simulations and two evaluation methods using shear cell (SC) simulations.

Friction coefficient pair	HSS	SC - torque method [eq. (32)]	SC - local friction method
$(\mu,\mu_r) = (0.25,0.00)$	0.337 ± 0.012	0.235 ± 0.004	0.344 ± 0.023
$(\mu,\mu_r) = (0.25,0.20)$	0.461 ± 0.018	0.375 ± 0.005	0.474 ± 0.032
$(\mu,\mu_r) = (0.45,0.15)$	0.463 ± 0.018	0.418 ± 0.004	0.478 ± 0.051

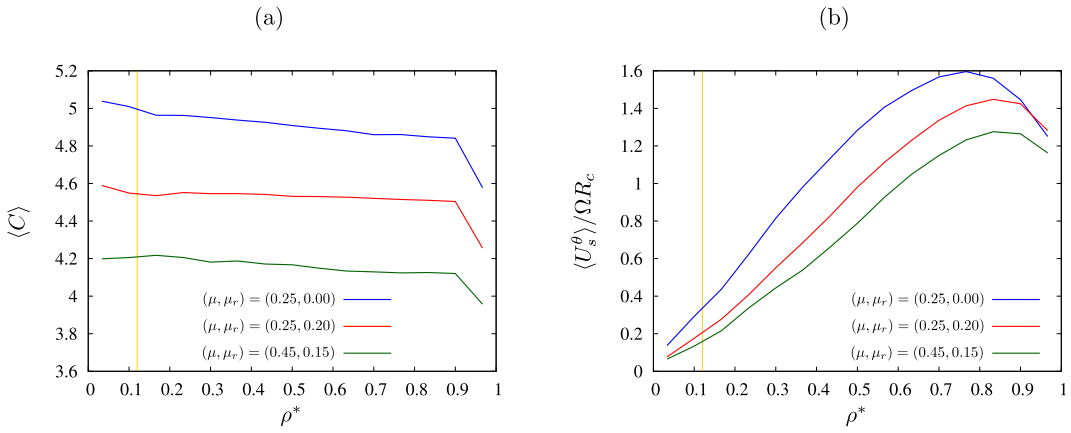

Fig. 12. Comparison of time-averaged local variables as a function of the dimensionless radial co-ordinate for different friction coefficient pairs: (a) - contact number $\langle C \rangle$; (b) - solid velocity normalised with shear head tip speed $\frac{\langle U_s^\theta \rangle}{\Omega R_c}$. The yellow lines represent the boundary of the central "no-shearing" zone. (For interpretation of the references to colour in this figure legend, the reader is referred to the web version of this article.)

shows equivalence between the two methods for predicting the shear strength of the material. It can also be seen that the method using eq. (32) in a similar way to the actual experimental process, is insufficient and consistently under-predicts bulk friction. This is possibly due to the manner in which the simulation is conducted, with pressure being applied by the base rather than the shear head itself.

The time-averaged local contact number $\langle C \rangle$ as a function of the dimensionless radial co-ordinate for each friction coefficient pairing is shown in Fig. 12-a. Near the centre of the cell the particles remain in their initial solid state with a slightly raised contact number. The contact number then decreases slightly across the radial length and drops significantly at the wall, as is expected due to wall-particle contacts not contributing to the contact number. It is possible to see clear differences between friction coefficient pairs, with the couple $(\mu, \mu_r) = (0.45, 0.15)$ having the lowest values along the whole radial length, then $(\mu, \mu_r) = (0.45, 0.15)$, and finally the case without rolling friction shows the highest contact number throughout. It would seem that greater inhibition of motion - particularly sliding motion - prevents particles packing as closely.

Fig. 12-b reports the time-averaged local solid velocity in the angular axis, normalised by shear head tip speed $\langle U_s^\theta \rangle / \Omega R_c$, as a function of the dimensionless radial co-ordinate. For each pair the same trend is observed, with a linear increase from the centre to a critical point near the wall, at which velocity drops slightly. It should be noted that the case without rolling friction reaches this critical point further from the wall than the 'correct' and the potential pairs, and also sees particle velocity drop more significantly approaching the wall. The case without rolling friction logically has the highest velocity profile due to motion being less inhibited.

These results also show that the case with higher sliding friction shows the lowest velocity profile, and the closest to approaching the shear head tip speed. Higher sliding friction means the particles in the shear deformation zone are more likely to match the velocity of the particles above which are inducing shear. They are effectively being 'dragged' as a result of sliding friction, and this hypotheses would appear to be supported by the force network branch vector direction PDFs (Figs. 10-a,b,c). As was discussed previously, the contact vector distribution suggests a greater influence of the shear head. It is likely that if inter-particle friction coefficients were increased further - particularly sliding friction - the velocity profile peak would approach 1 i.e. the shear head tip speed.

6. Conclusions

The main objective of this work was to investigate the frictional properties of a dry particle assembly of glass beads. To attain this objective, experimental studies of the shearing behaviour using the FT4 shear cell apparatus have been coupled with extensive DEM shear simulations with both homogeneous simple shear and shear cell flow configurations. This was done in order to understand which inter-particle friction coefficients in DEM simulations could reproduce the bulk friction coefficient found with the experimental apparatus, and what the effect of selecting different inter-particle friction coefficients was on obtained simulation results.

It was found that with HSS simulations, it was not possible to reproduce the experimental value of μ^*_{exp} unless a rolling friction model was implemented. HSS simulations on their own also leave an infinite set of possibly correct pairs of rolling and sliding friction coefficients. A correct pair can be readily identified in most cases by using another experiment to fix either sliding or rolling friction. In this study, the coefficient of sliding friction was fixed by performing the sliding test experiments. Investigation of the force network in these simulations showed inclusion of rolling friction produced a more realistic outcome, with the strong network orientated firmly in the direction of the major stress and having a less isotropic distribution.

The HSS simulations identified inter-particle friction coefficient pairings capable of reproducing the bulk friction coefficent but were unable to show any differences in obtained results for the force networks between pairings. To show more clearly the impact of friction coefficient selection, a more realistic case was simulated. To this end, the FT4 shear cell used for experiments was simulated numerically using the 'correct' pair and another potential calibration pair, as well as a pair without rolling friction. The results showed clear differences between each pairing. Analysis of the force networks showed equivalency between the shear cell simulations and HSS simulations with regards to the distribution and orientation of the SN in the direction of the major stress. A clear difference was found between the two methods with regards to the WN however, with the shear cell simulations showing a complete absence of the weakest contacts. This absence was attributed to the wall taking over the role of supporting the strong network, and supported by the fact the weak network was now also orientated in the direction of the major stress. Differences between pairings were also shown, with the pair without rolling friction showing a radial orientation of SN contacts not seen with the correct pair and additional potential calibration

pair. The pair with higher sliding friction showed a significant effect of the shear head on the SN orientations.

In addition to the force network, the shear cell simulations showed differences between pairs in radial profiles of local friction, contact number, and velocity. The results for local friction, although profiles varied slightly, showed good agreement with values for bulk friction obtained with HSS simulations. In terms of contact number, the results showed that increasing both rolling and sliding friction decreased the contact number, and inhibited the ability of particles to pack closely. A similar trend was seen with velocity, with increasing sliding and rolling friction reducing solid velocity, approaching the shear head tip speed.

In this work much effort was spent to correctly calibrate the numerical model with experimental results, and to understand that a correct calibration should focus, not only on capturing the overall response of a system, but also on capturing the physics at the particle scale. The use of mathematical modelling is justified by the high quantity and quality of information able to be retrieved from the numerical model. Much of this data is difficult or impossible to obtain by experimental means, or limited to a very low number of particles. It remains infeasible in most cases to rely on more complicated, more computationally expensive interaction models which could reduce the efforts necessary for the correct calibration of inter-particle friction coefficients. In particular, improved rolling friction models are needed in DEM modelling because it is not possible in most cases to experimentally measure the coefficient of rolling friction.

Many of the hypotheses in this work would be further supported by conducting the outlined procedure on a different particle system. Although this was not conducted at this stage, it is a potential avenue for future work. It is also planned to use the calibrated system to simulate the mechanical behaviour of glass beads in the presence of cohesion. Specifically, it is intended to use a coating liquid to induce liquid bridges between particles. For these systems, the configuration of the contact number (in which the inter-particle friction coefficient pair play a major role) has to be correctly captured by the DEM modelling in order to approximate the experimental system. It is hoped that the procedure outlined in this work can therefore go some way to easing the associated difficulties with calibration, and eventually shed valuable light on complex particle-particle interactions.

Declaration of Competing Interests

The authors declare that they have no known competing financial interests or personal relationships that could have appeared to influence the work reported in this paper.

Acknowledgements

The support from the EPSRC, UK (Grant No. EP/N034066/1) is kindly acknowledged.

Appendix A. Appendices

A.1. Results for other friction models

Many rolling friction models are available in literature to account for the rolling friction phenomena, and in this work four different approaches were tested. The first is the constant directional torque (CDT) model, developed by Zhou et al. [54]:

$$M_\mu = \mu_r r^* F_{c,n} \frac{\overleftarrow{\omega}_\mu}{|\overleftarrow{\omega}_\mu|}, \tag{37}$$

where M_μ is the rolling friction torque, μ_r is the rolling friction parameter, r^* is the equivalent radius of the two particles in contact, $F_{c,n}$ is the contact normal force and $\overleftarrow{\omega}_\mu$ is the relative rotational velocity. This rolling friction model is one of the most used in DEM algorithms [22,41,42] due to its simplicity and the low number of parameters to calibrate. The second model is that of Ai et al. [3] outlined in the main discussion, taking into consideration two values of $\eta_r = 0$ and 0.3. The third model considered is that developed by Kazuyoshi and Masanobu [34] (EPSD2), which is also based on a spring approach, but the spring constant is computed as:

$$M_\mu = \begin{cases} k_\mu^{EPSD2}\theta_\mu \text{ if } k_t r^{*2}\theta_\mu \le \mu_r r^* F_{c,n} \\ \mu_r r^* F_{c,n} \text{ otherwise.} \end{cases} \tag{38}$$

$$k_\mu^{EPSD2} = k_t r^{*2} \tag{39}$$

This model comes from dimensional considerations of sliding friction torque and rolling friction torque. To test these models, several simulations were run with the algorithm explained in section 4 while varying the friction coefficient pairs. The results for μ^* for each model and friction coefficient pair are shown in Table 7.

The CDT model does not seem to have any influence on μ^*. This effect has also been reported by other research groups [42] and can probably be attributed to the definition of the rolling friction torque direction $\frac{\overleftarrow{\omega}_\mu}{|\overleftarrow{\omega}_\mu|}$. In fact, as reported by Ai et al. [3], in the case of low rolling velocity the CDT model is inaccurate. For the EPSD model, η_r does not seem to have any effect on μ^*. With regards to the EPSD2 model, it seems to yield a slightly higher μ^* compared to the EPSD model for the same friction coefficients. This can probably be explained by the difference in springs constants and by taking into consideration the ratio:

$$R_r = \frac{k_\mu^{EPSD}}{k_\mu^{EPSD2}} = 0.75\mu_r^2 \frac{2-\nu}{1+\nu} \tag{40}$$

For the values of damping coefficient μ_r considered in this work, $k_{\bar{\mu}}^{EPSD}$ is about two orders of magnitude less than k_μ^{EPSD2}, but for higher values of μ_r these two models would approach the same value of μ^*.

A.2. Effect of the wall on shear cell simulations

In addition to the shear cell simulations in Section 5.3, a sensitivity analysis of the wall friction was performed. The need for this section, despite wall friction being readily measurable experimentally, comes from how the shear cell was simulated. While in the real shear cell the shear head will apply both normal pressure and shear, in the simulation case the bottom boundary (base) has been used to apply the normal

Table 7
Internal friction coefficient μ^* as a function of sliding friction coefficient μ and rolling friction coefficient μ_r pairs for different rolling friction models.

	CDT	EPSD; $\eta_r = 0$	EPSD; $\eta_r = 0.3$	EPSD2
$(\mu, \mu_r) = (0.15, 0.00)$	0.301	0.301	0.301	0.301
$(\mu, \mu_r) = (0.25, 0.00)$	0.337	0.337	0.337	0.337
$(\mu, \mu_r) = (0.35, 0.00)$	0.352	0.352	0.352	0.352
$(\mu, \mu_r) = (0.45, 0.00)$	0.362	0.362	0.362	0.362
$(\mu, \mu_r) = (0.15, 0.05)$	0.300	0.336	0.338	0.349
$(\mu, \mu_r) = (0.25, 0.05)$	0.340	0.377	0.375	0.386
$(\mu, \mu_r) = (0.35, 0.05)$	0.358	0.395	0.393	0.401
$(\mu, \mu_r) = (0.45, 0.05)$	0.364	0.402	0.401	0.410
$(\mu, \mu_r) = (0.15, 0.10)$	0.300	0.369	0.369	0.377
$(\mu, \mu_r) = (0.25, 0.10)$	0.334	0.413	0.413	0.420
$(\mu, \mu_r) = (0.35, 0.10)$	0.357	0.430	0.427	0.436
$(\mu, \mu_r) = (0.45, 0.10)$	0.462	0.434	0.440	0.442
$(\mu, \mu_r) = (0.15, 0.15)$	0.301	0.387	0.386	0.389
$(\mu, \mu_r) = (0.25, 0.15)$	0.338	0.441	0.440	0.442
$(\mu, \mu_r) = (0.35, 0.15)$	0.353	0.456	0.457	0.459
$(\mu, \mu_r) = (0.45, 0.15)$	0.363	0.462	0.463	0.464

Table 8
Coefficient of internal friction μ^* as a function of the wall friction coefficient μ^w.

	μ^*
$\mu^w = 0.10$	0.478 ± 0.051
$\mu^w = 0.15$	0.430 ± 0.015
$\mu^w = 0.20$	0.385 ± 0.012

pressure. This leads to normal pressure being applied inversely and discrepancies between simulation wall friction and experimental wall friction.

There are several walls in the simulation environment that could be investigated, namely the shear head, the base, and the cylindrical cup. The friction between the shear head and the particles is not expected to play a major role in the simulation since most of the shear is induced by the movement of the blades. Similarly, the friction between the particles and the base will not influence the simulation much since these particles are in the static region. The wall friction coefficient between the cylindrical cup and the particles μ^w is important however, as this wall interacts directly with particles undergoing shear. For this reason, it was decided to be the focus of the sensitivity analysis.

The shear cell simulation properties will mostly remain as outlined in Section 5.3. Where the simulations in this section differ is four wall friction coefficients will be used: $\mu^w = [0.05; 0.10; 0.15; 0.20]$, and the only friction coefficient pair used will be the pair $(\mu, \mu_r) = (0.45, 0.15)$. The simulation using $\mu^w = 0.05$ failed, with the whole particle system rotating like a rigid body without any shearing applied to the particle system. For the other simulations, it was possible to apply shearing to the particle system and to evaluate the coefficient of internal friction, for which the results are presented in Table 8.

The wall friction coefficient was found to clearly impact the value of μ^* obtained, however no influence was found on H_γ. To understand why the wall friction coefficient μ^w impacts μ^*, the compression stress applied at the base σ^{zz} was compared with the time-averaged local stresses in the shearing deformation zone $\langle\sigma^{zz}\rangle$, through the definition of the dimensionless normal stress $\langle\sigma^{zz,*}\rangle$:

$$\langle\sigma^{zz,*}\rangle = \frac{\langle\sigma^{zz}\rangle}{\sigma^{zz}} \tag{41}$$

Fig. 13 displays the evolution of the dimensionless normal stresses $\langle\sigma^{zz,*}\rangle$ along the radial direction in the shear deformation zone for different values of μ^w.

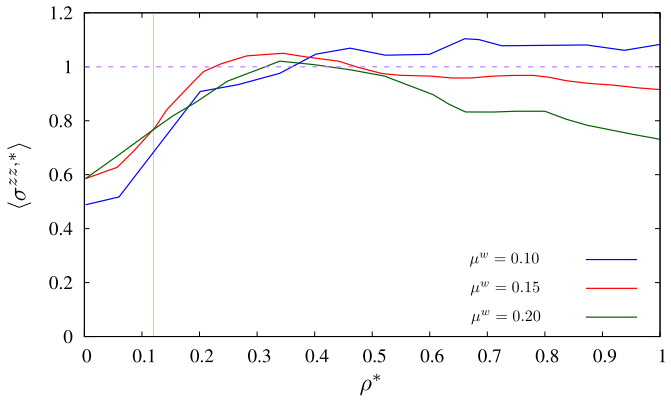

Fig. 13. Time-averaged dimensionless axial stress profile as a function of the dimensionless radial co-ordinate ρ^* for $\mu^w = [0.10; 0.15; 0.20]$. The yellow line represents the central "no-shearing" zone. (For interpretation of the references to colour in this figure legend, the reader is referred to the web version of this article.)

The compression stresses, as expected, are very low in the centre for all wall friction coefficient values and rise rapidly in the shearing zone. In the shearing zone the compression profile is highly influenced by wall friction. While for $\mu^w = 0.10$ and $\mu^w = 0.15$ the dimensionless compression stresses are very near to the stress value applied by the base, for $\mu^w = 0.20$ the profile shows heavy losses at the wall because of the expansion of the weak network near the cylindrical cup. The zone near the cylindrical cup wall is also the part of the shear cell where the shear head applies most of the deformation and hence the measure of the coefficient of internal friction can be greatly affected by the characteristics of the cylindrical cup. Care must therefore be taken when using an annular shear cell, where the homogeneity of the profile can be affected more by wall friction.

References

[1] L. Aarons, S. Sundaresan, Shear flow of assemblies of cohesive and non-cohesive granular materials, Powder Technol. 169 (2006) 10–21.
[2] I. Agnolin, J.N. Roux, Internal states of model isotropic granular packings. I. Assembling process, geometry, and contact networks, Phys. Rev. E 76 (2007) 061302.
[3] J. Ai, J.F. Chen, J.M. Rotter, J.Y. Ooi, Assessment of rolling resistance models in discrete element simulations, Powder Technol. 206 (2011) 269–282.
[4] E. Andò, S.A. Hall, G. Viggiani, J. Desrues, P. Bésuelle, Grain-scale experimental investigation of localised deformation in sand: a discrete particle tracking approach, Acta Geotech. 7 (2012) 1–13.
[5] B. Andreotti, Y. Forterre, O. Pouliquen, Granular Media: Between Fluid and Solid, Cambridge University Press, 2013.
[6] M. Badetti, A. Fall, F. Chevoir, J.N. Roux, Shear strength of wet granular materials: Macroscopic cohesion and effective stress, Eur. Phys. J. E 41 (2018) 68.
[7] M. Badetti, A. Fall, D. Hautemayou, F. Chevoir, P. Aimedieu, S. Rodts, J.N. Roux, Rheology and microstructure of unsaturated wet granular materials: Experiments and simulations, J. Rheol. 62 (2018) 1175–1186.
[8] J. Baker, F. Guillard, B. Marks, I. Einav, X-ray rheography uncovers planar granular flows despite non-planar walls, Nat. Commun. 9 (2018) 5119.
[9] J. Bridgwater, W. Foo, D. Stephens, Particle mixing and segregation in failure zones—theory and experiment, Powder Technol. 41 (1985) 147–158.
[10] H. de Cagny, A. Fall, M.M. Denn, D. Bonn, Local rheology of suspensions and dry granular materials, J. Rheol. 59 (2015) 957–969.
[11] C.S. Campbell, Rapid granular flows, Annu. Rev. Fluid Mech. 22 (1990) 57–90.
[12] I. Cavarretta, C. O'Sullivan, E. Ibraim, M. Lings, S. Hamlin, D.M. Wood, Characterization of artificial spherical particles for DEM validation studies, Particuology 10 (2012) 209–220.
[13] S. Chialvo, J. Sun, S. Sundaresan, Bridging the rheology of granular flows in three regimes, Phys. Rev. E Stat. Nonlinear Soft Matter Phys. 85 (2012) 21305.
[14] Y. Chung, J. Ooi, J. Favier, Measurement of mechanical properties of agricultural grains for de models, 17th ASCE Engineering Mechanics Conference. Netwark, USA, 2004.
[15] C.J. Coetzee, D.N.J. Els, Calibration of discrete element parameters and the modelling of silo discharge and bucket filling, Comput. Electron. Agric. 65 (2009) 198–212.
[16] P.A. Cundall, O.D.L. Strack, A discrete numerical model for granular assemblies, Géotechnique 29 (1979) 47–65.
[17] A. Di Renzo, F.P. Di Maio, Comparison of contact-force models for the simulation of collisions in DEM-based granular flow codes, Chem. Eng. Sci. 59 (2004) 525–541.
[18] T.G. Drake, Granular flow: physical experiments and their implications for microstructural theories, J. Fluid Mech. 225 (1991) 121–152.
[19] N. Estrada, A. Taboada, F. Radjaï, Shear strength and force transmission in granular media with rolling resistance, Phys. Rev. E 78 (2008), 021301.
[20] R. Freeman, Measuring the flow properties of consolidated, conditioned and aerated powders — A comparative study using a powder rheometer and a rotational shear cell, Powder Technol. 174 (2007) 25–33.
[21] I. Goldhirsch, Rapid granular flows, Annu. Rev. Fluid Mech. 35 (2003) 267–293.
[22] C. Goniva, C. Kloss, N.G. Deen, J.A.M. Kuipers, S. Pirker, Influence of rolling friction on single spout fluidized bed simulation, Particuology 10 (2012) 582–591.
[23] C. Goniva, C. Kloss, A. Hager, S. Pirker, An open source CFD-DEM perspective, Proceedings of OpenFOAM Workshop, Göteborg 2010, pp. 1–10.
[24] A.P. Grima, P.W. Wypych, Discrete element simulations of granular pile formation, Eng. Comput. Bradford 28 (2011) 314–339.
[25] P.S. Grover, Modeling of rolling resistance test data, SAE Trans. (1998) 497–506.
[26] D.E. Hall, J.C. Moreland, Fundamentals of rolling resistance, Rubber Chem. Technol. 74 (2001) 525–539.
[27] S.S. Hsiau, H.W. Jang, Measurements of velocity fluctuations of granular materials in a shear cell, Exp. Thermal Fluid Sci. 17 (1998) 202–209.
[28] S.S. Hsiau, J.Y. Shiu, W.L. Yang, L.S. Lu, Influence of internal friction on transport properties in sheared granular flows, AICHE J. 52 (2006) 3592–3599.
[29] S.S. Hsiau, W.L. Yang, Transport property measurements in sheared granular flows, Chem. Eng. Sci. 60 (2005) 187–199.
[30] M.J. Jiang, H.S. Yu, D. Harris, A novel discrete model for granular material incorporating rolling resistance, Comput. Geotech. 32 (2005) 340–357.
[31] K.L. Johnson, K.L. Johnson, Contact Mechanics, Cambridge University Press, 1987.

[32] M. Johnstone, J. Ooi, Calibration of dem models using rotating drum and confined compression measurements, 6th World Congress on Particle Technology, Nuremberg, Germany, 2010.
[33] P. Jop, Y. Forterre, O. Pouliquen, A constitutive law for dense granular flows, Nature 441 (2006) 727.
[34] I. Kazuyoshi, O. Masanobu, Rolling resistance at contacts in simulation of shear band development by DEM, J. Eng. Mech. 124 (1998) 285–292.
[35] C. Kloss, C. Goniva, A. Hager, S. Amberger, S. Pirker, Models, algorithms and validation for opensource DEM and CFD–DEM, Prog. Computat. Fluid Dynam Int. J. 12 (2012) 140–152.
[36] F. Lacombe, S. Zapperi, H.J. Herrmann, Dilatancy and friction in sheared granular media, Eur. Phys. J. E 2 (2000) 181ArXiv: cond-mat/9908359.
[37] A.W. Lees, S.F. Edwards, The computer study of transport processes under extreme conditions, J. Phys. C Solid State Phys. 5 (1972) 1921–1928.
[38] M. Leturia, M. Benali, S. Lagarde, I. Ronga, K. Saleh, Characterization of flow properties of cohesive powders: A comparative study of traditional and new testing methods, Powder Technol. 253 (2014) 406–423.
[39] L.Y. Lin, D.E. Kim, W.K. Kim, S.C. Jun, Friction and wear characteristics of multi-layer graphene films investigated by atomic force microscopy, Surf. Coat. Technol. 205 (2011) 4864–4869.
[40] H. Louati, Experimental and Numerical Study of Humid Granular Material : Influence of Liquid Content in Quasi-Static Regime, Ph.D Ecole des Mines d'Albi-Carmaux, 2016.
[41] R. Maione, S.K. De Richter, G. Mauviel, G. Wild, Axial segregation of a binary mixture in a rotating tumbler with non-spherical particles: Experiments and DEM model validation, Powder Technol. 306 (2017) 120–129.
[42] A.S. Persson, G. Frenning, The influence of rolling friction on the shear behaviour of non-cohesive pharmaceutical granules – An experimental and numerical investigation, Eur. J. Pharm. Sci. 49 (2013) 241–250.
[43] P.E. Peyneau, J.N. Roux, Frictionless bead packs have macroscopic friction, but no dilatancy, Phys. Rev. E 78 (2008), 011307.
[44] O. Pouliquen, F. Chevoir, Dense flows of dry granular material, Comp. Rend. Phys. 3 (2002) 163–175.
[45] F. Radjaï, M. Jean, J.J. Moreau, S. Roux, Force distributions in dense two-dimensional granular systems, Phys. Rev. Lett. 77 (1996) 274–277.
[46] F. Radjaï, D.E. Wolf, M. Jean, J.J. Moreau, Bimodal character of stress transmission in granular packings, Phys. Rev. Lett. 80 (1998) 61–64.
[47] J. Schwedes, Review on testers for measuring flow properties of bulk solids, Granul. Matter 5 (2003) 1–43.
[48] R. Stannarius, Magnetic resonance imaging of granular materials, Rev. Sci. Instrum. 88 (2017), 051806.
[49] J. Sun, S. Sundaresan, A constitutive model with microstructure evolution for flow of rate-independent granular materials, J. Fluid Mech. 682 (2011) 590–616.
[50] Z. Syed, M. Tekeste, D. White, A coupled sliding and rolling friction model for DEM calibration, J. Terrramech. 72 (2017) 9–20.
[51] S.P. Timoshenko, J.N. Goodier, H.N. Abramson, Theory of elasticity (3rd Ed.), J. Appl. Mech. 37 (1970) 888.
[52] M. Urbakh, J. Klafter, D. Gourdon, J. Israelachvili, The nonlinear nature of friction, Nature 430 (2004) 525.
[53] D.M. Wood, G.S. Boulton, J.M. Rotter, C. Thornton, S.J. Anthony, Quasi–static deformation of particulate media, Phil. Trans. R. Soc. Lond. Ser. A: Math. Phys. Eng. Sci. 356 (1998) 2763–2782.
[54] Y.C. Zhou, B.D. Wright, R.Y. Yang, B.H. Xu, A.B. Yu, Rolling friction in the dynamic simulation of sandpile formation, Phys. A Stat. Mech. Appl. 269 (1999) 536–553.